Slippage on a particle-laden liquid-gas interface in textured microchannels

Anvesh Gaddam[1], Amit Agrawal[1], Suhas S. Joshi[1], Mark C. Thompson[2]

[1]Department of Mechanical Engineering, Indian Institute of Technology Bombay, Powai, Mumbai 400076, India.

[2]Fluids Laboratory for Aeronautical and Industrial Research (*FLAIR*), Department of Mechanical and Aerospace Engineering, Monash University, Clayton 3800, Australia.

Abstract

We report results from numerical simulations of the flow past a liquid-gas interface embedded with solid particles. This work mainly focuses on the reduction in *effective slip length* by solid particles adsorbed at the liquid-gas interface in textured microchannels. Initially, we present numerical simulations past transverse ribs with single cylindrical particles on the liquid-gas interface positioned at the midpoints between ribs. The reduction in the effective slip length (or slip loss) with respect to the particle-free interface as a function of gas fraction, constriction ratio, particle position and contact angle was quantified. A significant slip loss (~20-80%) was induced, owing to acceleration-deceleration cycles experienced by the liquid advecting across the particle-laden liquid-gas interface. This rendered such a particle-laden interface of a textured microchannel to be ineffective as compared to a completely wetted textured microchannel under certain conditions. Furthermore, the effective slip length for two bi-dimensional surface texturing patterns, viz. posts and holes, with their interfaces embedded with spherical particles was also investigated. Due to the unbounded liquid-gas interface in the surface with posts, unlike the one with holes, the slip loss was observed to be less for the former than the latter. The simulations enabled the validity of scaling laws to be extended to textured microchannels containing particle-laden interfaces. In overview, even a small number of inert solid particles adsorbed on a liquid-gas interface will considerably reduce the effective slip length in textured microchannels. Since a stringent requirement of cleanliness is often difficult to achieve in real-world applications, our results suggest that significant drag reduction using textured microchannels might be challenging to realize in practice.

Keywords: Cassie-Baxter state, effective slip length, liquid-gas interface, particle-laden interface, textured microchannel, Wenzel state

1. INTRODUCTION

Measured in terms of pressure drop (ΔP), the resistance to transporting a liquid through a microchannel decreases rapidly with the characteristic cross-stream length (l) [1]: $\Delta P \sim 1/l^4$. This is attributed to the increase in surface area to volume ratio at microscales. One way to partially overcome this issue is by texturing the inner surfaces of the microchannel. Surface texturing causes the liquid state to exist in one of two states. These can be described by either liquid flow over entrapped gas in cavities formed by the textures, known as the *Cassie-Baxter state* (CB), or flow with the liquid filling the cavities formed by the textures, referred to as the *Wenzel state* (W). In the former, a reduction in the pressure drop is due to velocity slip at liquid-gas interface. A reduction in pressure drop in the latter is ascribed to an increase in the effective flow area. Both experiments and theory suggest that the Cassie-Baxter state offer a lower resistance to the liquid flow than the Wenzel state[2-5].

Navier proposed that the *slip velocity* (u_s) at a solid-liquid surface is proportional to the local rate of shear stress ($\partial u_s/\partial y$) [6]. The constant of proportionality λ is termed as slip length, which is the imaginary distance underneath the surface at which the no-slip boundary condition is recovered. Experimental studies and molecular dynamics simulations on solid-liquid interfaces have reported slip lengths in the range of tens of nanometers[7-9]. However, a significant fractional reduction in the pressure drop in a microchannel is only possible if the slip length is of the order of the characteristic length scale of the microchannel. Textured microchannels consisting of alternate no-shear and no-slip regions are known to yield high slip lengths[10]. Lauga and Stone[11] introduced the *effective slip length* as a useful metric to compare the reduction in pressure drop on textures of different geometries and sizes. Analytical studies formulated simple predictive expressions for the effective slip length for one-dimensional (longitudinal and transverse ribs) and two-dimensional textures (posts and holes) as a function of gas fraction (ratio of shear-free area to the total projected area) [11-12]. Numerical works augmented these expressions for the effective slip length by including gas fraction, Reynolds number and constriction ratio (ratio of microchannel height to pattern width) [13-14]. Traditionally, the liquid-gas interface is assumed to be flat and shear-free in these works. These idealized conditions result in over prediction of the effective slip length. Therefore, subsequent analytical and numerical works accounted for the interface deformation and dissipation between the liquid and gas phases to amend the previously reported correlations[15-16]. For example,

the ratio of effective slip length for longitudinal to transverse ribs with dissipation in both the phases no longer amounts to a value of two as predicted in the idealized case. On the contrary, the liquid-gas interface deformation is not always detrimental in terms of the effective slip length. Theoretical works showed that the effective slip length increases to an optimal value when the liquid-gas interface bows into the liquid flow field, which is further supported by experiments[17-20]. However, a deformation beyond the optimal value leads to a negative effective slip length due to blockage caused by the protruding interface into the core flow.

Experiments on flow past textured surfaces have however revealed contrasting outcomes. Lee et al.[21] reported slip lengths closer to the theoretical limit on textured surfaces in a shear-driven flow. Tsai et al.[22] observed a deviation of greater than 50% in experimentally measured slip length from theory, in pressure-driven flow through textured microchannels. The liquid-gas interface deformation was partly attributed to this nonconformity. In some experimental studies where the global average quantities such as pressure drop or volumetric flow rate were measured, the Wenzel state was observed to be better than the Cassie-Baxter state[23-25]. With the help of experiments and numerical simulations, these works deduced that the liquid-gas interface behaves like a partial no-slip boundary. Local velocity measurements in flow through textured microchannels were also shown to exhibit no-slip behaviour at the liquid-gas interface[26-27]. The authors presumed that the deposition of impurities on the liquid-gas interface carried by the liquid, from the external system or the substrate itself could be the cause of this interfacial immobility. A more recent study showed that a substantial decrease in slip length occurs even at a low concentration of surfactant adsorbed at the liquid-gas interface[28]. A change in boundary condition from full-slip to partial slip was also observed with an addition of a small amount of salts[29-30]. In summary, any particle or surfactant contamination on the liquid-gas interface may lead to a significant reduction of slip length.

Solid particles (or colloidal particles, as they are often called in the literature) are ubiquitous in closed channel flows in biological, chemical and industrial systems[31-33]. Colloidal particles are categorized based on their architecture and dimensionality (3D - spherical, 2D - flat disc and 1D – cylinder) with a typical size distribution ranging from one nanometer to tens of micrometers. These particles tend to accumulate spontaneously at the fluid-fluid interfaces irrespective of the chemical composition on their surface[34]. If a chemically active solid particle is trapped at the liquid-gas interface, a change in surface tension occurs along the interface. A gradient in the surface tension

along the liquid-gas interface leads to Marangoni stresses, which oppose the liquid flow over the interface. However, not all the colloidal particles are chemically active through their surface. It is hypothesized that even an inert solid particle can influence the flow behaviour at the liquid-gas interface.

To this end, we numerically investigate the effect of a solid particle embedded at the liquid-gas interface on the effective slip length in textured microchannels. This paper begins with numerical simulations past one dimensional textures (transverse ribs) with a cylindrical particle situated on the liquid-gas interface. The effects of particle contact angle, position on the liquid-gas interface, microchannel constriction ratio and gas fraction on the effective slip length are presented. Subsequently, the simulations are extended to bi-dimensional textures (posts and holes) with a spherical particle adsorbed on the liquid-gas interface. Furthermore, we invoke the 'dirty' interface argument to explain why the experimental pressure drop in the Wenzel state was observed to be less than the Cassie-Baxter state in the literature.

2. MEHODOLOGY

2.1 Physical description of the problem

An infinitely wide microchannel containing texture elements on the bottom wall was considered in this study, while the top wall was set to be smooth. Fig. 1(a) shows a single module of a microchannel containing a one-dimensional texture (transverse ribs) on the bottom wall with a cylindrical particle situated on the liquid-gas interface. The nomenclature and boundary conditions of the computational module are shown in the figure. As the velocity field repeats from one module to the next, periodic boundary conditions were imposed at the module inlet and outlet. For a typical air-water system inside a textured microchannel, the very low viscosity ratio between the two phases ($\mu_a/\mu_w \approx 0.01$, where, μ_a and μ_w are viscosities of air and water respectively) allowed us to impose a no-shear boundary condition at the interface. That is, no gas phase was involved in the numerical simulations where the Cassie-Baxter state exists and the cylindrical particle was reduced to a circular bump on the liquid-gas interface for transverse ribs. A no-slip boundary condition was applied on rest of the surfaces including the top wall, rib, and cylindrical particle. The liquid-gas interface was assumed to be flat owing to a sufficiently small Capillary number (Ca) in the

simulations. Similarly, in the limit of small capillary number, the rotation of particle on the interface is negligible[35].

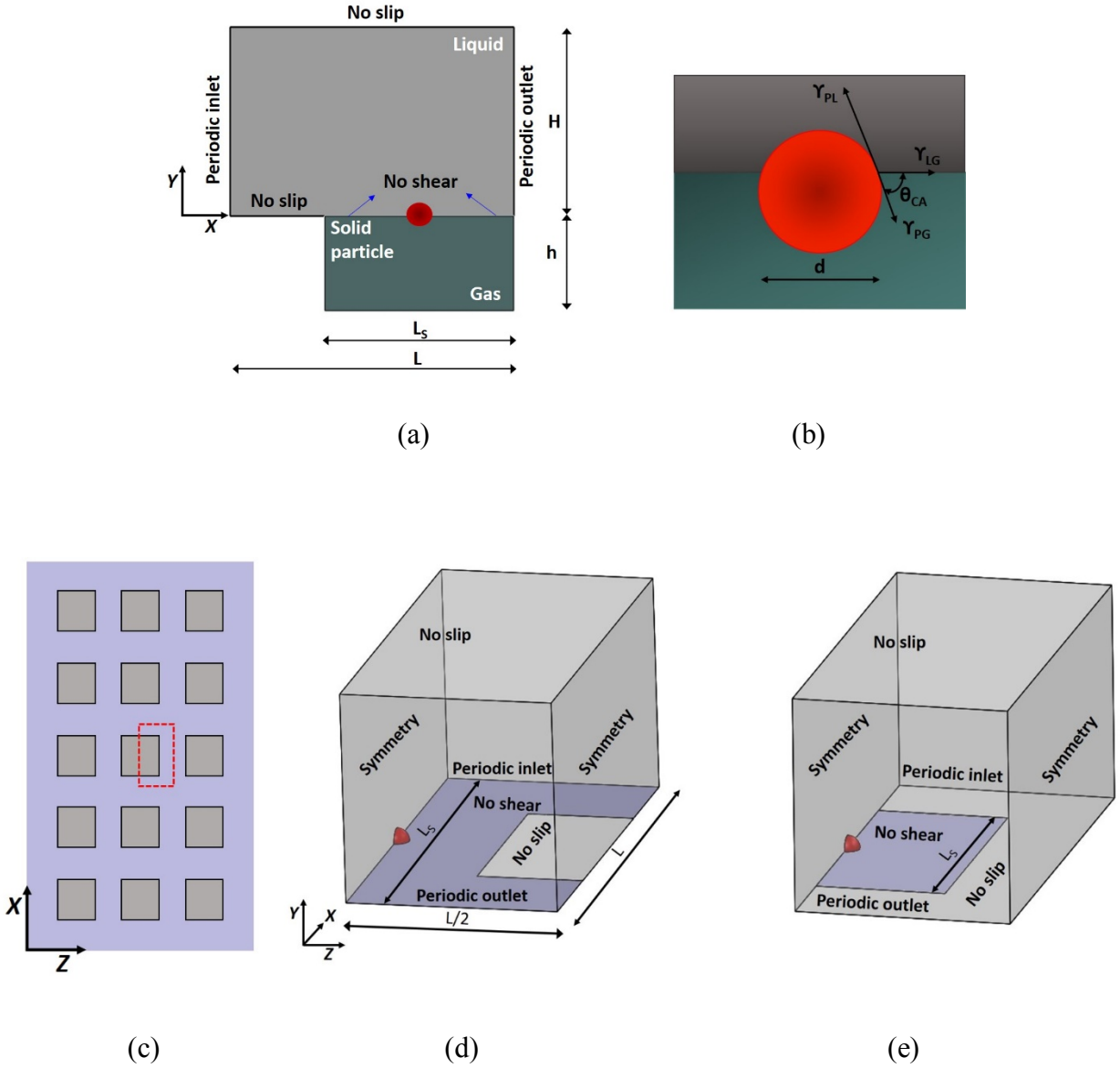

Figure 1: (a) Computational module with nomenclature and boundary conditions for transverse ribs. (**b)** Contact angle and interfacial tensions for the embedded particle at the interface. (**c)** Liquid-gas interface at the posts top surface for bi-dimensional textures. The region highlighted by red dashed line was chosen for the numerical simulation domain. (**d)** Computational module with appropriate boundary conditions for posts. (**e)** Computational module with appropriate boundary conditions for holes. A one-quarter portion of the spherical particle is shown in red in (**d) and (e)** on one of the symmetry planes.

Furthermore, the typical size distribution of colloidal particles (generally < 10 μm) endorses that the capillary forces on a particle trapped at the interface is orders of magnitude greater than the weight of the particle. Therefore, the liquid-gas interface around the particle was assumed to be locally flat. Micro/nano-particles adsorbed at an interface with a contact angle closer to 90° possess the free energy of adsorption several orders of magnitude greater than the thermal energy[34]. This favours an irreversible attachment of particles at the interfaces. Thus, the contact angle (θ_{CA}) of the particle was fixed at 90° in the simulations, unless stated otherwise. The particle contact angle was defined as an angle between the tangent to the particle surface (into the gas phase) and the interface. as illustrated in Fig. 1(b).

Owing to the periodicity and symmetry of the bi-dimensional texture configuration (posts and holes) inside the microchannel in the X and Z directions, the region illustrated in Fig. 1(c) was chosen for the numerical simulations. The computational domain with nomenclature and appropriate boundary conditions for posts and holes is illustrated in Fig. 1(d) and (e) respectively. In the flow direction (X-direction), periodic conditions were imposed at the inlet ($X = 0$) and the outlet ($X = L$). Due to a mirror symmetry in transverse direction (Z), a symmetry boundary condition was applied at $Z = 0$ and $L/2$ planes. The spherical particle was positioned at the liquid-gas interface on one of the symmetry planes for the posts and holes simulations, as shown in Fig. 1(d) and (e). As noted earlier, the liquid-gas interface was assumed to be flat and shear-free, while rest of the surfaces were considered to be no-slip.

2.2 Calculation of flow parameters

The relevant geometrical parameters in this study are the gas fraction (δ), constriction ratio (ε) and cavity aspect ratio (κ). The gas fraction is defined as the ratio of no-shear area to the total area of the module. For instance, the gas fraction in the case of transverse ribs is L_S/L whereas, in case of posts it is expressed as L_S^2/L^2. The constriction ratio is defined as the ratio of module height (H) to its width (L) and the cavity aspect ratio is the ratio of cavity height (h) to its width (L_S). Note that the cavity aspect ratio is only relevant in those simulations where the flow exists in the Wenzel state. The pressure gradient value obtained from the simulations was converted into an effective slip length through the following equations

$$fRe = \frac{D_H^3 \rho \Delta P}{\dot{m} \mu L}, \tag{1}$$

$$\frac{\lambda}{H} = \frac{32}{fRe} - \frac{1}{3}, \tag{2}$$

$$\frac{\lambda}{L} = \varepsilon \times \frac{\lambda}{H}, \tag{3}$$

where ΔP is the pressure drop, $\dot{m}$ is the mass flow rate, L is the length of the domain, fRe is the *Poiseuille number* and λ is the effective slip length. Note that in the subsequent sections, the effective slip length normalized by the module height (λ/H) will be termed the effective slip length itself, while the effective slip length normalized by the module length (λ/L) will be called the normalized effective slip length.

2.3 Numerical details

The liquid flow inside the textured microchannel was assumed to be steady, incompressible and laminar with constant thermo-physical properties. Therefore, the following continuity and momentum equations are applicable for this scenario:

$$\nabla . \mathbf{u} = 0, \tag{4}$$

$$\rho \frac{\partial \mathbf{u}}{\partial t} + \rho \left(\mathbf{u} . \nabla \mathbf{u} \right) = -\nabla P + \mu \nabla^2 \mathbf{u}, \tag{5}$$

where the velocity field $\mathbf{u} = [u, v, w]$ corresponds to the spatial field $\mathbf{X} = [X, Y, Z]$.

The geometries were modeled and meshed in ANSYS ICEM CFD 14.0 and the governing equations (4)–(5) were solved using ANSYS FLUENT 14.0. All the simulations were carried out in the Stokes flow limit ($Re \leq 1$), to ensure $Ca \ll 1$. Here, $Re = \rho u D_H / \mu$ is the Reynolds number and $Ca = \mu u / \gamma_{LG}$ is the capillary number. In these equations, ρ is the density of liquid, u is the velocity in the X-direction, D_H is the hydraulic dimeter, μ is the viscosity of liquid, and γ_{LG} is the surface tension along the liquid-gas interface. Abrupt acceleration-deceleration cycles were expected in the computational module at the textured surface due to a change in the boundary condition from no-shear to no-slip at the three-phase contact line (at the edge of the texture and in the vicinity of particle). Therefore, the mesh was locally refined at $Y = 0$ in the module at the beginning of the simulation through the region adaption method. A second-order upwind scheme was adopted for discretizing the convective and diffusive terms, while the SIMPLE algorithm was

chosen for the pressure-velocity coupling. Once the mass flow rate corresponding to the desired *Re* specified at the inlet was reached, the continuity and velocity residuals in the simulations were allowed to converge until they reached 10^{-4}. Thereafter, a dynamic velocity gradient-based mesh adaption method was followed in the simulations to attain a grid independent solution until the desired convergence criteria or 10^{-9} was achieved. This technique adds/deletes cells depending on the local velocity gradient to ensure that the flow field is well captured at convergence of the process. As an indication of its computational efficiency, the difference in predicted pressure drop values for a particular case of ε =1and δ = 0.5 without a particle was less than 0.5% between an extremely fine mesh consisting of 160,000 elements and an adapted mesh consisting of just 10,800 elements.

3. ONE-DIMENSIONAL TEXTURE WITH A CYLINDRICAL PARTICLE

In this section, the numerical results for flow past transverse ribs containing a cylindrical particle on the liquid-gas interface are presented. A particle situated on the liquid-gas interface will be termed as 'adsorbed particle' in the following discussion. Also note that the terms 'liquid-gas interface' and 'interface' will be used interchangeably in this paper. An effect of the adsorbed particle on the effective slip length with respect to module geometric parameters such as gas fraction and constriction ratio were studied, followed by particle-related parameters such as particle position on the liquid-gas interface and the contact angle.

3.1 Validation of the results

To investigate the validity of numerical simulations, the numerically obtained normalized effective slip length for flow in the Cassie-Baxter state and the Wenzel state were compared with the corresponding analytical results. Teo et al.[36] expressed the normalized effective slip length for flow past transverse ribs as a function of gas fraction as:

$$\frac{\lambda}{L} = \frac{1}{2\pi} \ln\left[\sec\left(\frac{\delta\pi}{2}\right) \right]. \qquad (6)$$

The above relation was derived for a shear flow past transverse ribs in the Stokes regime and is valid for a relatively large separation between the top wall and the textured bottom wall ($\varepsilon >> 1$).

Therefore, the simulations were carried out for the case where ε = 10 at a very low Reynolds number (Re = 0.01). In a similar manner, the numerically obtained normalized effective slip length in the Wenzel state was compared with the phenomenological relationship provided by Woolford et al.[13] The simulations for the Wenzel state were carried out keeping κ = 1, in view of the limitations imposed on the phenomenological relationship. Fig. 2(a) shows the comparison of the numerical and analytical normalized effective slip length for both the Cassie-Baxter state and the Wenzel state. The numerical results were in good agreement with the analytical results with a maximum deviation of 3%.

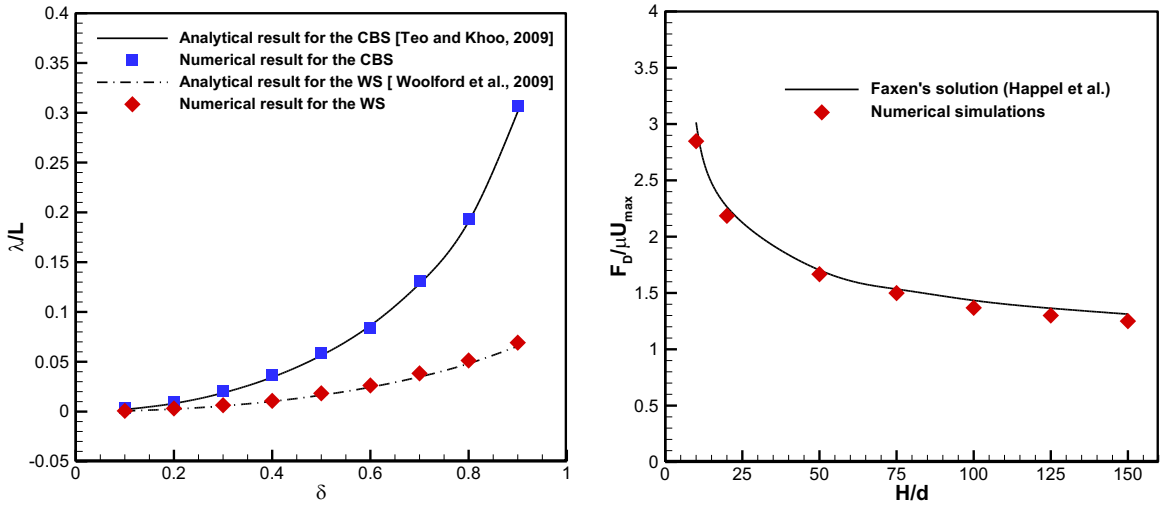

(a) (b)

Figure 2: (a) Comparison of the numerically obtained effective slip length for flow in the Cassie-Baxter state and the Wenzel state, across a microchannel containing transverse ribs on the bottom wall with analytical results at ε = 10. The simulations for the Wenzel state are carried out at κ = 1. **(b)** Comparison of numerically calculated normalized drag force on a solid particle positioned on a liquid-gas interface (for θ_{CA} = 90°) with Faxen's analytical solution[37].

Further, the accuracy of simulations for the particle-laden interface were validated through Faxen's power series analytical solution. The drag force (F_D) on a cylindrical particle traversing along the

axis of an infinitely wide channel is expressed in terms of viscosity, diameter of particle, channel height and center-line velocity (U_{max}) as[37]:

$$\frac{F_D}{\mu U_{\max}} = \frac{4\pi}{\ln(2H/d) - 0.9157 + 1.7244(d/2H)^2 - 1.7302(d/2H)^4} . \quad (7)$$

In the present work, a flow past an adsorbed particle with θ_{CA} = 90° in a microchannel was numerically simulated. The computational module was similar to that shown in Fig. 1(a) without a rib. The simulations were carried out for H/d values ranging from 10 to 150. As the no-shear boundary condition ($\partial u/\partial y = 0$) at the interface is physically identical to a symmetry boundary condition ($\partial u/\partial y = 0$), the numerically calculated drag force on a cylindrical particle is half of that calculated by Eq. 7. Fig. 2(b) shows good agreement between the normalized drag forces calculated both analytically and numerically.

3.2 Influence of gas fraction

We begin our analysis by examining the influence of an adsorbed particle on the effective slip length at different gas fractions when the particle is situated at the mid-section of the cavity (x/L_S = 0.5) on the liquid-gas interface. The particle contact angle was fixed at 90° in these simulations with a constriction ratio of unity. The particle dimensions for this case correspond to H/d = 100, i.e., for instance, a microchannel with a height of 100 μm has an adsorbed particle of 1 μm diameter at all gas fractions.

Fig. 3(a) shows the effective slip length on the interface with an adsorbed particle along with the condition where flow exists in the Cassie-Baxter state and the Wenzel state as the two limiting cases. Under normal circumstances, it is reasonable to envisage the effective slip length has upper and lower limits corresponding to whether the flow exists in the Cassie-Baxter state or the Wenzel state respectively. As mentioned earlier, the cavity aspect ratio was kept constant, i.e., κ = 1, for those simulations where the Wenzel state exists. We can define a particle-free interface as a '*clean*' interface and particle-laden interface as a '*dirty*' interface. The curve representing the effective slip length for a 'dirty' interface rightly lies between the low and upper limits of the effective slip length. It is also apparent from the figure that an adsorbed particle has considerably reduced the effective slip length on the interface with respect to a 'clean' interface. Further, the curve showing the effective slip length for a 'dirty' interface is closer to the lower limit of the effective slip length.

An adsorbed particle reduces the no-shear area of the module, which leads to a reduction in the effective slip length. The percentage reduction in the no-shear area due to a particle is plotted in Fig. 3(b) for each gas fraction. Importantly, it is evident from the figure that a reduction in the no-shear area is not so significant (≤ 10%) for the given geometric parameters ($\varepsilon = 1$ and $H/d = 100$).

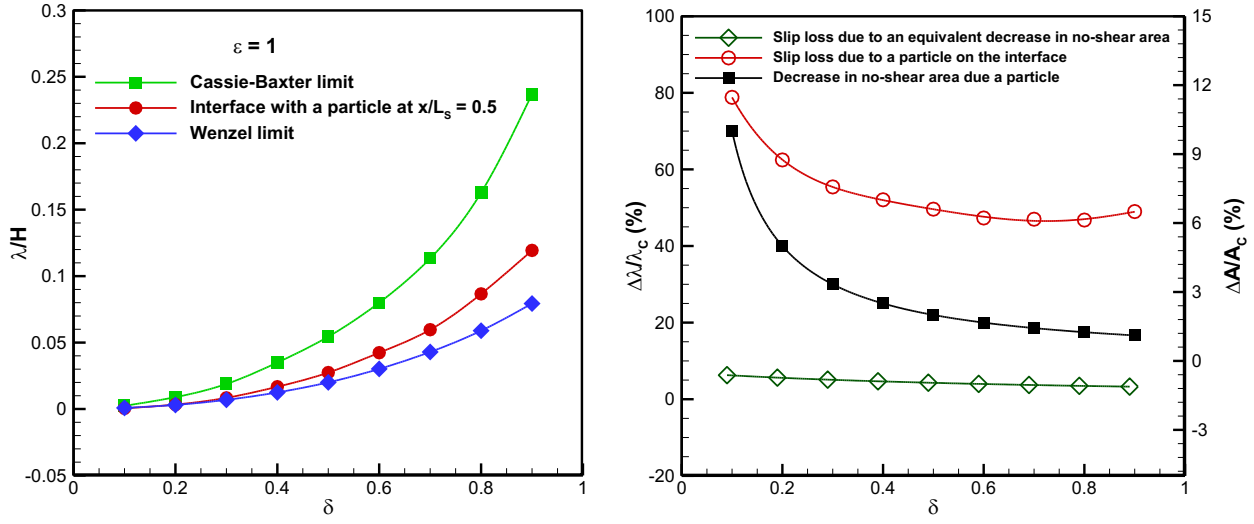

(a) (b)

Figure 3: (a) Effective slip length as a function of gas fraction for flow in the Cassie-Baxter state (green squares), the Wenzel state (blue diamonds) and for interface with an adsorbed solid particle positioned at $x/L_S = 0.5$ for $\theta_{CA} = 90^o$ (red circles). (**b)** Percentage reduction in slip length for a particle-laden interface (hollow red circles) and for an interface with reduced no-shear area (hollow dark green diamonds) is shown. Percentage reduction in no-shear area is also shown.

Therefore, it is required to compare the magnitude of reduction in the effective slip length in two different cases to understand the flow behaviour at the liquid-gas interface. The slip loss (or percentage reduction in the effective slip length) is calculated by following expression:

$$\frac{\Delta\lambda}{\lambda_C} = \frac{\lambda_C - \lambda_P}{\lambda_C} \times 100 \qquad (8)$$

Here, λ_C and λ_P are the slip lengths for 'clean' and 'dirty' interfaces respectively. In the first case, the effect of the adsorbed particle is shown as the slip loss with the gas fraction (red circles) in Fig 3(b). A significant reduction in the effective slip length (45 – 80%) can be seen from the figure.

In the second case, simulations were carried out on a computational module with an equivalent increase in rib dimension (L-L_S) corresponding to the particle diameter for each gas fraction. The slip loss for this case is minor (3 – 6 %) as shown in the figure. Therefore, an adsorbed particle significantly influences the flow behaviour at the interface.

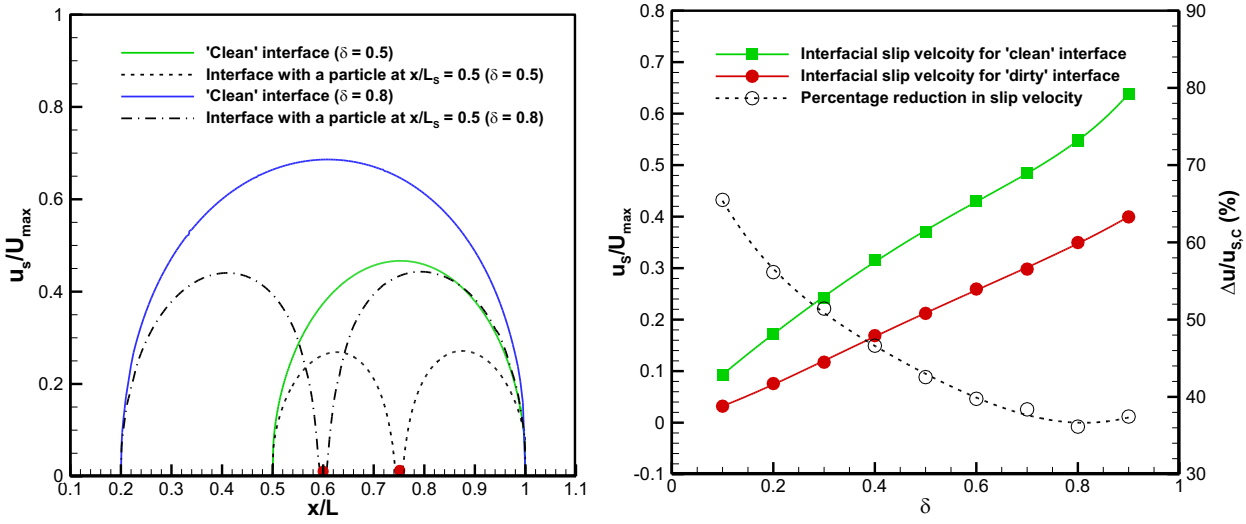

(a) (b)

Figure 4: (**a)** Normalized interfacial slip velocity for ‘clean’ and ‘dirty’ interfaces at $\delta = 0.5$ and 0.8. (**b)** Normalized interfacial slip velocity for ‘clean’ and ‘dirty’ interfaces plotted as a function of gas fraction.

To understand the local hydrodynamics on an interface with and without a particle, the slip velocity on the interface at each gas fraction is calculated. Fig. 4(a) shows the normalized interfacial velocity for ‘clean’ and ‘dirty’ interfaces at two different gas fractions ($\delta = 0.5$ and 0.8). Here, the interfacial velocity is normalized by the center-line velocity (U_{max}) of the microchannel. It is apparent from the figure that the liquid accelerates to a maximum value at the mid-section of the interface and then decelerates to a minimum value on the rib surface for a ‘clean’ interface.

However, there exist two acceleration-deceleration cycles for a ‘dirty’ interface. That is, the liquid accelerates to a maximum value between the rib surface and the solid particle and the cycle repeats until the liquid passes from one cavity to another cavity. This leads to an overall reduction in the average slip velocity on a ‘dirty’ interface. The magnitude of average normalized slip velocity with respect to gas fraction is plotted in Fig. 4(b) for ‘clean’ and ‘dirty’ interfaces. It is evident that the

slip velocity is significantly reduced (35 – 65 %) by introducing a particle on the liquid-gas interface. Note that, the curves representing percentage reduction in slip length and slip velocity are showing similar behavior, as seen from Figs. 3(b) and 4(b).

3.3 Influence of constriction ratio

The constriction effect on the effective slip length for both 'clean' and 'dirty' interfaces has been studied in this work by maintaining a smooth upper wall. Figs. 5(a) and b show a variation in the effective slip length with the constriction ratio at two different gas fractions (δ = 0.5 and 0.9). In the limit of large constriction ratio ($\varepsilon >> 1$), the flow behaviour on the bottom textured surface will not be affected by the upper wall. Therefore, the effective slip length for a 'clean' interface was shown to increase linearly with a decrease in constriction ratio for $\varepsilon > 0.5$ and set to level off for $\varepsilon < 0.5$, for both the gas fractions. A similar trend is noticed for an interface with a particle adsorbed at $x/L_S = 0.5$. However, an increase in number of particles to three situated equidistantly on the interface (x/L_S = 0.25, 0.5 and 0.75), recovered the linear behaviour of the effective slip length with the constriction ratio.

A variation in the slip loss with the constriction ratio for the interfaces with one and three particles is plotted in Figs. 5(c) and (d) at two different gas fractions. It is apparent that an increase in the number of particles on an interface from one to three doubled the slip loss for both the gas fractions. A change in no-shear area due to one and three adsorbed particles is 2% and 6% respectively for δ = 0.5, the corresponding values are 1% and 3% for δ = 0.9. That is, a minor change in the no-shear area due to adsorbed particles leads to a significant slip loss (attaining a maximum value of ~ 80%). Introducing more particles on an interface leads to an increase in the number of interfacial acceleration-deceleration cycles. Therefore, the average interfacial slip velocity decreases further, leading to a more slip loss for an interface with three particles. This situation is identical to increasing the number of textures in a microchannel for a given gas fraction, where a similar observation was made in the earlier works[38]. That is, the friction factor was found to increase as the liquid experiences more acceleration-deceleration cycles. Also, the slip loss is steeply decreasing with a decrease in constriction ratio for $\varepsilon < 1$. This indicates that a textured microchannel of 10 μm in height loses its effectiveness by ~ 20%, whereas a textured microchannel of 200 μm in height loses its effectiveness by ~ 45% with an adsorbed particle of 1 μm diameter.

Further, curves representing the slip loss asymptote to ~ 45% and ~ 80% for interfaces with one particle and three particles respectively for $\varepsilon > 1$. Although textured microchannels with $\varepsilon < 1$ yield slip lengths as large as the microchannel height, the pressure required to drive the liquid through such a textured microchannel exceeds the critical pressure that the interface can sustain[39].

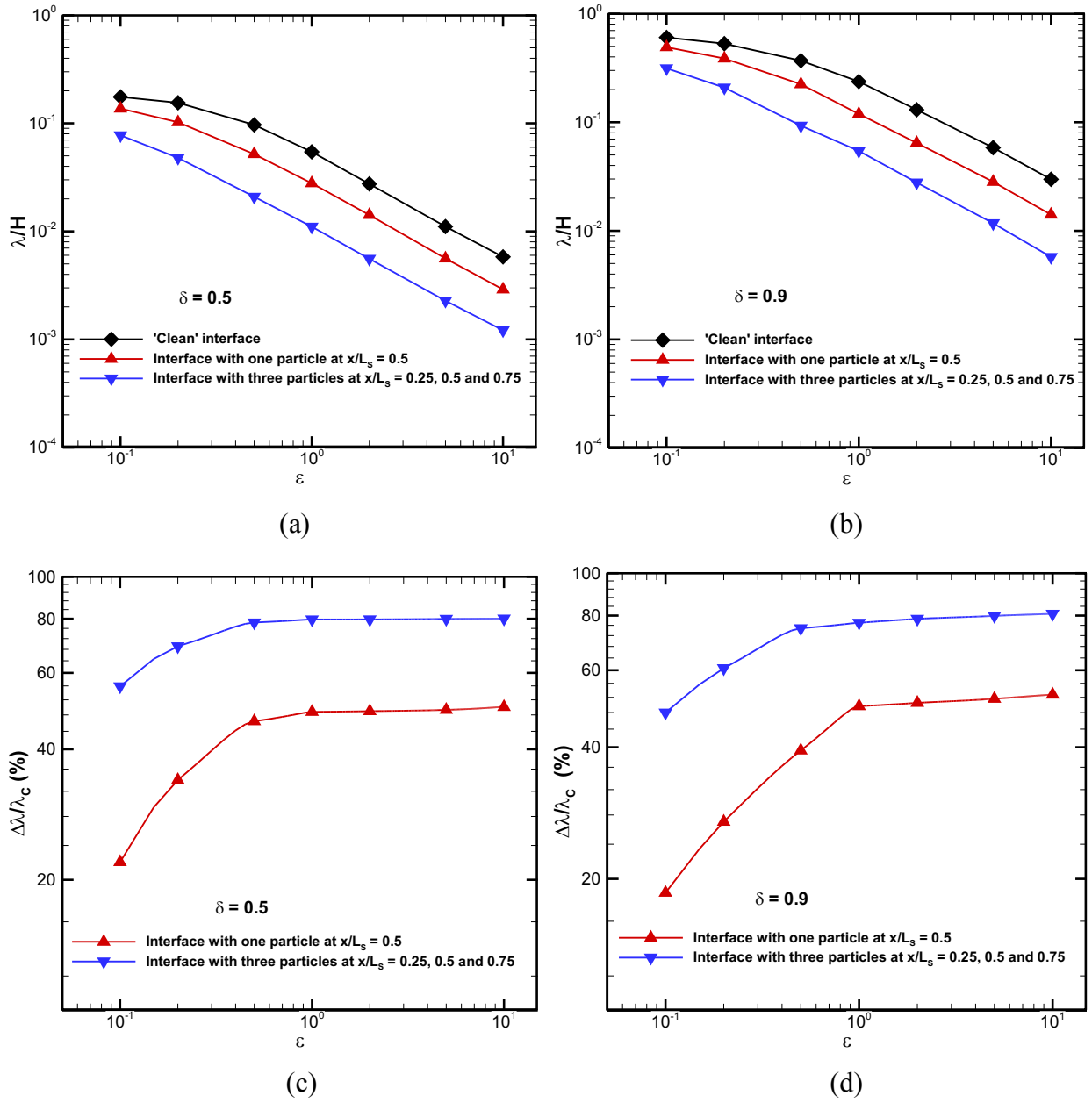

Figure 5: (a-b) Variation of the effective slip length with the constriction ratio, with and without a solid particle on the interface for two different gas fractions (δ = 0.5 and 0.9). **(c-d)** The effective slip length data for an interface with solid particle(s) re-cast in the form of percentage reduction in slip length with respect to a 'clean' interface.

This leads to flooding of the gas cavities by the liquid, which limits their usefulness. Therefore, textured microchannels with low constriction ratios are impractical, even though the negative influence of the adsorbed particle on the effective slip length is vanishing at lower constriction ratios.

3.4 Influence of particle position and contact angle

As explained earlier, a particle positioned at the middle of the interface (x/L_S = 0.5) reduces the average interfacial slip velocity as the liquid experiences acceleration-deceleration cycles. In this case, the interfacial velocity is equally distributed on either side of the adsorbed particle. That is, the particle position dictates the distribution of the interfacial velocity. Fig. 6 shows the distribution of the interfacial velocity for a particle positioned at x/L_S = 0.1 and x/L_S = 0.5 for a gas fraction of 0.9. It is apparent that the distribution of the interfacial velocity varies when the particle is displaced from x/L_S = 0.5 to x/L_S = 0.1, with the maximum distribution occurring on the downstream side of the particle along the interface. The limiting case occurs if the particle is attached to the rib decreasing the no-shear area.

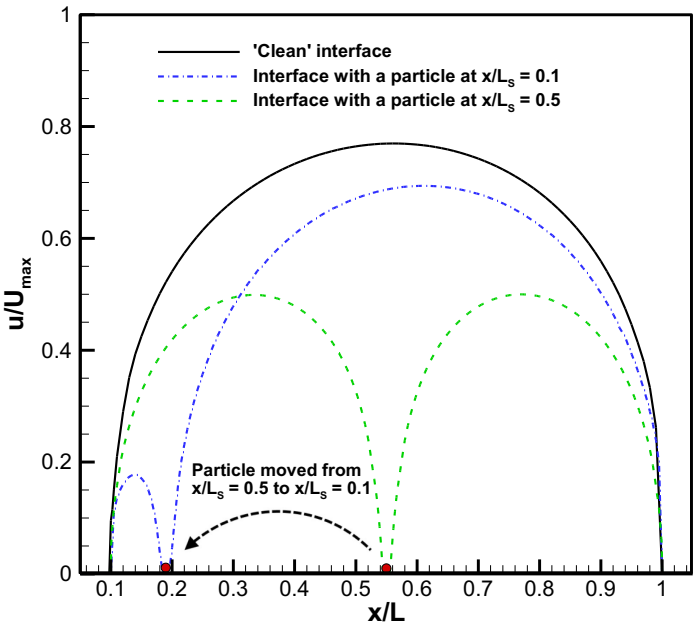

Figure 6: Distribution of normalized velocity on the interface for a 'clean' interface (black solid line), particle positioned at x/L_S = 0.5 (green dashed line) and particle positioned at x/L_S = 0.1 (blue dot dashed line) at δ = 0.9.

In this case, the slip loss is not very significant as explained through Fig. 3(b). The magnitude of slip loss at different constrictions ratios (ε = 0.1, 1 and 10) is plotted in Fig. 7 with respect to position of the particle on an interface for δ = 0.5 and 0.9. It is apparent that the slip loss drastically changes with the position of a particle for $\varepsilon \geq 1$. The slip loss attains a maximum value when the particle is positioned at the middle of the interface (x/L_S = 0.5). A change in position of the particle near to the rib decreases the slip loss to a limiting case of a rib of enlarged dimensions. However, the slip loss is not a strong function of the particle position for smaller constriction ratios ($\varepsilon \leq 1$), as shown in figure.

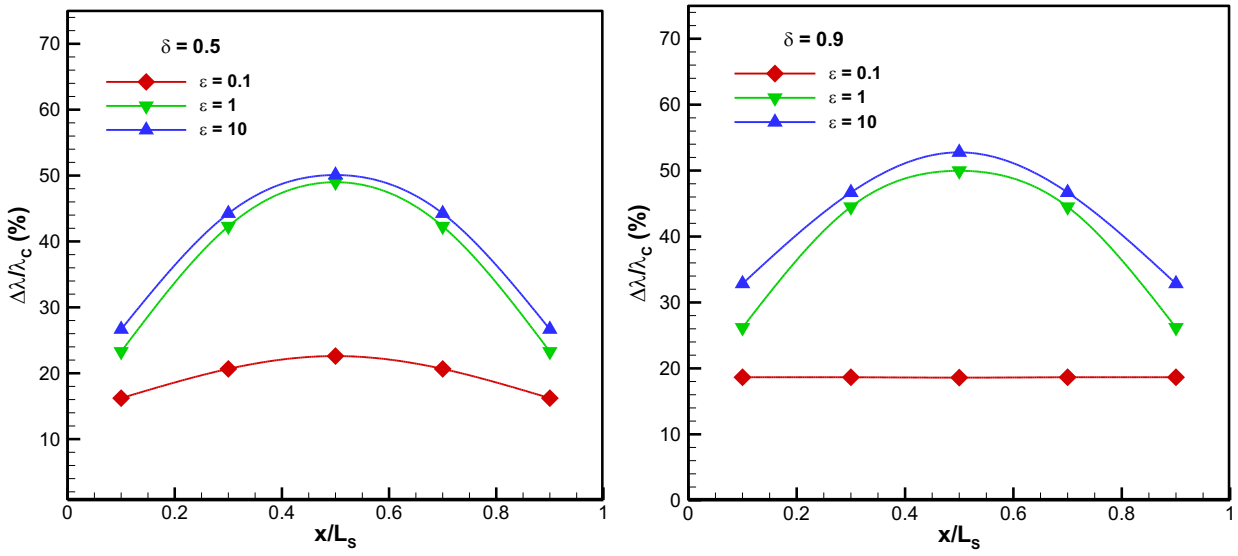

(a) (b)

Figure 7 (a-b): Percentage reduction in effective slip length with position at different constriction ratios for **(a)** δ = 0.5 and **(b)** δ = 0.9.

Although the particle contact angle is set to 90° as a limiting case in the present simulations, micro/ nanoparticles tend to adsorb at the interface at different immersion depth i.e., at a different contact angle due to their physical and chemical properties. For example, Janus particles belong to a class of interesting colloidal particles with two distinct surface regions of wettability[40]. An interaction

of these particles with the fluid-fluid interface varies depending on their architecture and amphiphilic nature[41-42]. Therefore, a set of simulations was carried out at different constriction

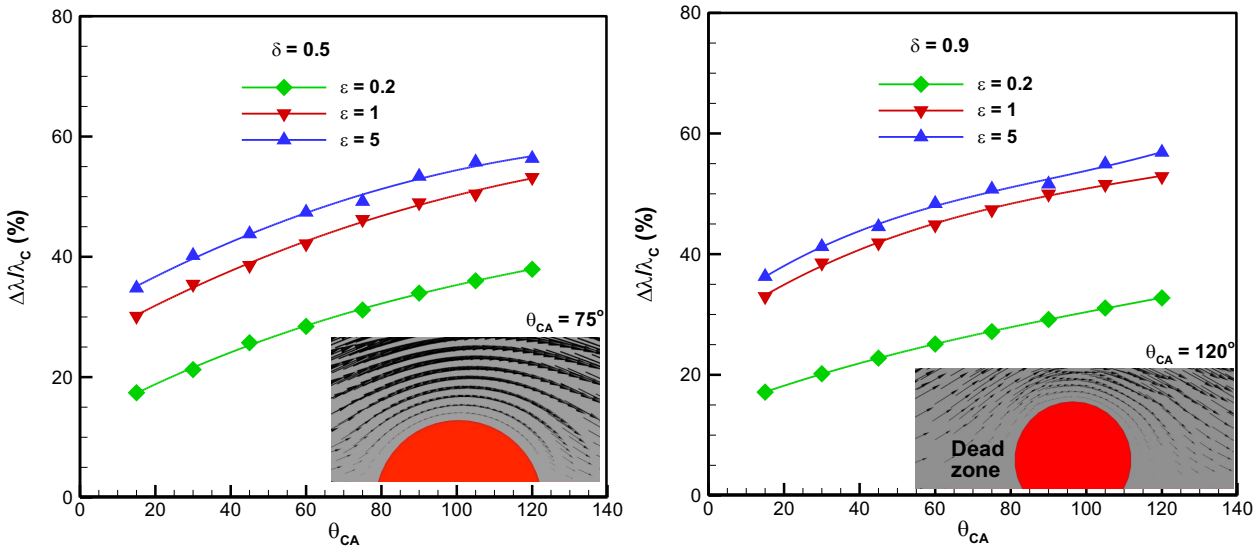

(a) (b)

Figure 8 (a-b): Percentage reduction in effective slip length with particle contact angle at different constriction ratios for **(a)** $\delta = 0.5$ and **(b)** $\delta = 0.9$. The flow behaviour near to the particle is shown in the inset for two different particle contact angles ($\theta_{CA} = 75^o$ and 120^o).

ratios ($\varepsilon = 0.2$, 1 and 5) and gas fractions ($\delta = 0.5$ and 0.9) by varying the contact angle ($15^o \leq \theta_{CA} \leq 120^o$).

The numerical results for the slip loss with respect to the particle contact angle are plotted in Fig. 8. It is clear that the slip loss increases with an increase in the particle contact angle. It should be noted that the no-shear area is a non-monotonic function of the particle contact angle. That is, the no-shear area initially decreases with an increase in the particle contact angle until 90^o and increases thereafter until 120^o. However, the particle pushes the streamlines into the liquid region with an increase in the particle contact angle, and leads to an immobilized liquid region (or dead zone) in the vicinity of the particle on the interface for $\theta_{CA} \geq 90^o$ as shown in the inset of Fig. 8. This is attributed to a monotonic increase in the slip loss for $15^o \leq \theta_{CA} \leq 120^o$.

3.5 Particle-laden Cassie-Baxter state versus the Wenzel state

As seen in section 3.3, an increase in number of particles on an interface led to a significant increase in the slip loss (~ 80%), even though the reduction in the no-shear area is minor. In some experimental studies, the pressure drop in the Wenzel state was observed to be less than the Cassie-

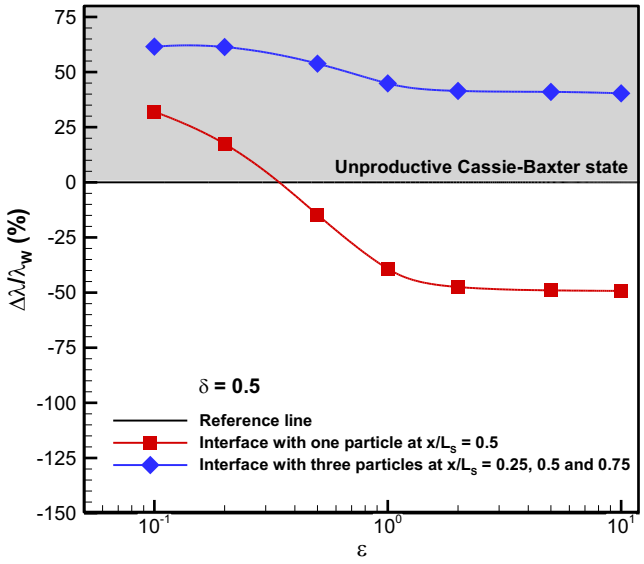

(a)

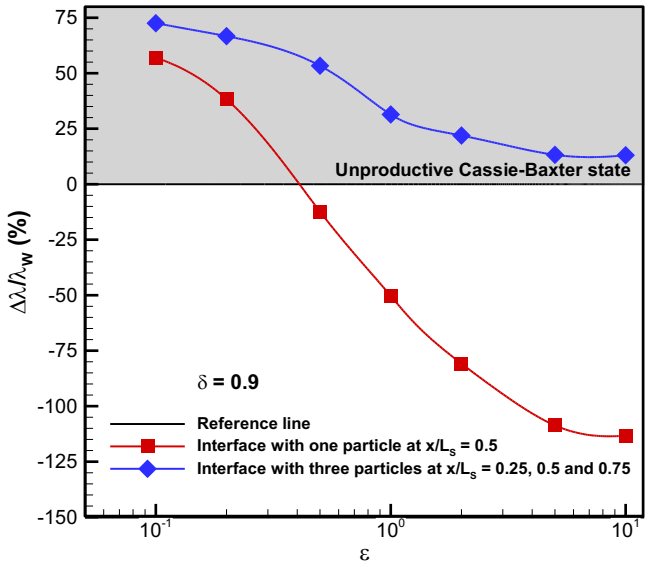

(b)

Figure 9 (a-b): Percentage reduction in the effective slip length calculated with respect to the Wenzel state versus constriction ratio for **(a)** $\delta = 0.5$ and **(b)** $\delta = 0.9$.

Baxter state[23-25]. The authors reasoned that the interface displayed a no-slip behaviour and attributed it to impurities deposited over the interface. It is interesting to note that no surfactants were employed in these studies, which could possibly induce Marangoni stresses. Therefore, it is reasonable to compare the effectiveness of the textured microchannel with particle-laden Cassie-Baxter state and the textured microchannel in which flow exists in the Wenzel state. As explained earlier, the simulations in the Wenzel state were carried out keeping $\kappa = 1$. In other words, the gas cavity height (h) corresponding to $\delta = 0.5$ and 0.9 are 50 μm and 90 μm respectively. The slip loss is calculated with respect to the Wenzel state according to the following expression:

$$\frac{\Delta\lambda}{\lambda_W} = \frac{\lambda_W - \lambda_P}{\lambda_W} \times 100. \qquad (9)$$

Fig. 9 shows the slip loss at two different gas fractions ($\delta = 0.5$ and 0.9) for interfaces with one and three particles. It is apparent from the figure that the textured microchannel in which flow exists in the Wenzel state is more advantageous than the textured microchannel in which the interface is covered with three particles. It is important to notice that there is only a minor change in the no-shear area of $\leq$ 6% due to particles resulting an ineffective non-wetted textured microchannel, as compared to a completely wetted textured microchannel. Even in the case of an interface with just one particle, the completely wetted textured microchannel is shown to be advantageous for $\varepsilon \leq 0.2$ at both the gas fractions.

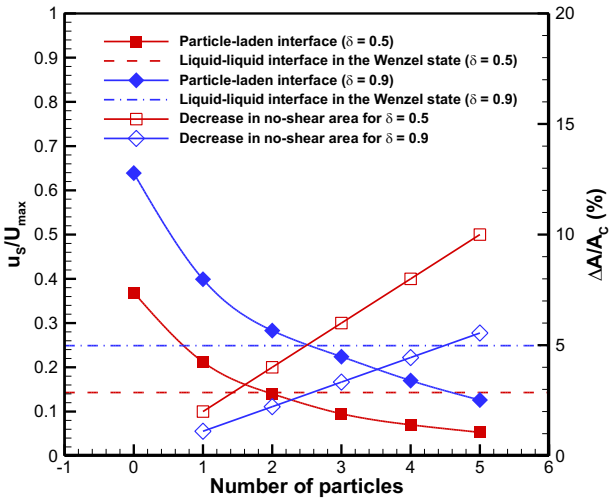

Figure 10: Percentage reduction in the normalized slip velocity with number of particles on interface for $\delta = 0.5$ and 0.9. Percentage reduction in no-shear area due to particles is also shown.

Fig. 10 shows a decrease in the average slip velocity with an increase in the number of particles on an interface at two gas fractions (δ = 0.5 and 0.9). The particles are positioned equidistantly on the interface in these simulations. The particle numbered zero in the figure corresponds to a 'clean' interface. The slip velocity at the liquid-liquid interface when the flow is in the Wenzel state is also included in the figure. It is observed that there is a clear loss of effectiveness of the non-wetted textured microchannel if the interface is covered with more than two particles in comparison to a completely wetted textured microchannel. Furthermore, increasing the number of particles on an interface leads to a no-slip behaviour, even if the corresponding decrease in the no-shear area is marginal ($\leq$ 10%).

4. BI-DIMENSIONAL TEXTURES WITH A SPHERICAL PARTICLE

In this section, numerical results for the flow past surfaces with posts and holes containing a spherical particle on the liquid-gas interface are presented. An effect of an adsorbed particle on the effective slip length with respect to gas fraction and orientation were studied. A validity of the scaling laws proposed by Ybert et al.[12] are extended for particle-laden interfaces for posts and holes by determining appropriate model coefficients.

4.1 Numerical validation

To investigate the validity of the three-dimensional numerical simulations, the numerically obtained normalized effective slip lengths for posts for flow in the Cassie-Baxter state are compared with the analytical formulae proposed by Enright et al.[43], as shown in Fig. 11a. The numerical simulations were carried out at a very low Reynolds number (Re = 0.01) and a large constriction ratio (ε = 80). Terms up to $O[(1\text{-}\delta)^{3/2}]$ were retained in the analytical formulae to validate the accuracy of the numerical simulations. Further, the numerical results were re-cast in the form of Eq. 10 to determine the appropriate coefficients in the scaling law proposed by Ybert et al.[12] A scaling law for the normalized effective slip length is expressed as:

$$\frac{\lambda}{L} = A(1-\delta)^{-1/2} - B \ . \qquad (10)$$

The coefficients (A, B) obtained through the numerical simulations are given in table-1. The results from the earlier numerical works are also included in the table for comparison.

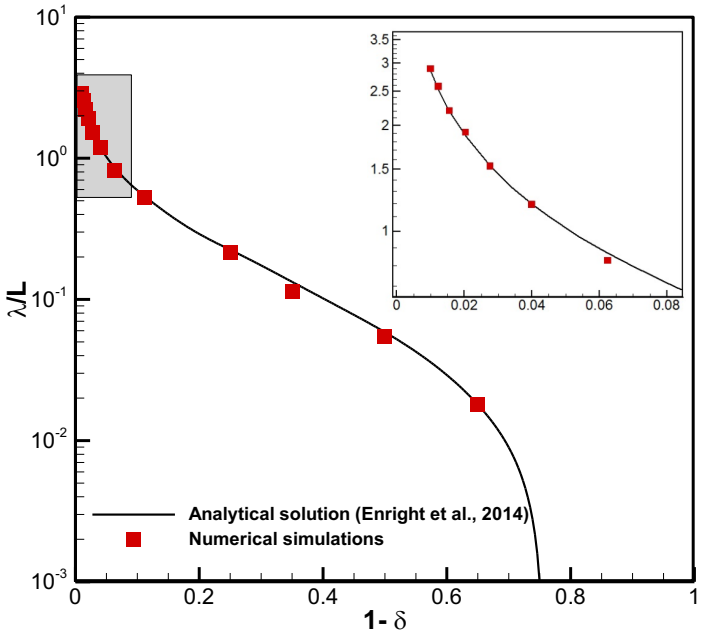

(a)

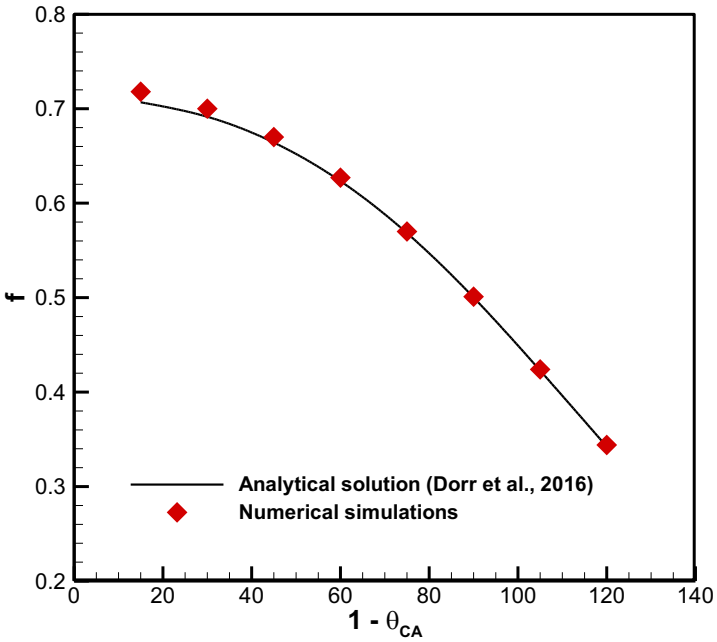

(b)

Figure 11: (**a)** Comparison of numerically obtained normalized (by module periodicity) effective slip length with the analytical solution provided by Enright et al. at all gas fractions. Numerical results at low gas fractions are shown in the inset. (**b)** Comparison of the numerical results for a spherical particle positioned on an interface (θ_{CA} = 90º and ε = 5) with the analytical solution.

Table-1: Comparison of coefficients in Eq. 10 from different numerical works.

Reference	A	B	Conditions
Cheng et al.[14]	0.336	0.450	Double-wall textured, ε = 2, *Re* = 1
Cowley et al.[44]	0.323	0.429	Double-wall textured, ε = 50, *Re* = 0.14
Enright et al.[43]	0.332	0.468	Double-wall textured, ε = 80
Present work	0.335	0.464	Single-wall textured, ε = 80, *Re* = 0.01

The numerical simulations for the textured microchannel with a particle-laden interface is validated through the analytical solution of drag force on a spherical particle traversing along a fluid-fluid interface as a function of the particle contact angle. An analytical formulae for the drag force on a particle at an interface, in the limit of a vanishing viscosity ratio of the two fluids, is expressed as[45]:

$$F_D = -6\pi\mu f U \ , \qquad (11)$$

where U is the particle velocity at the interface and f is a function of the particle contact angle. This is expressed as:

$$f = \frac{1}{2}\left[1 + \frac{9}{16}\cos(1-\theta_{CA}) - 0.139\cos^2(1-\theta_{CA}) + O(\cos^3(1-\theta_{CA}))\right] \ . \qquad (12)$$

A particle traversing along a liquid-gas interface with a velocity U is computationally identical to pressure-driven flow past a stationary particle adsorbed at a liquid-gas interface in a textured microchannel. Therefore, the simulations were carried out on a computational module similar to Fig. 1(c) without a post top surface at Re = 0.01 and ε = 5. Fig. 11(b) shows good agreement between the numerically obtained value of the function f and the analytical result obtained through the Eqs. 11 and 12.

4.2 Posts versus holes: Influence of gas fraction

The simulations are carried out on the post and hole configurations with one/three spherical particles positioned on the liquid-gas interface with $\theta_{CA} = 90^o$. The particles were arranged in the flow direction on the interface for the posts, i.e., at x/L_S = 0.5 for a single particle and at x/L_S =

0.25, 0.5, 0.75 for three particles. For holes, the particles were arranged normal to the flow direction i.e., at $x/L_S = 0.5$ for a single particle and at $z/L_S = 0.25, 0.5, 0.75$ for three particles.

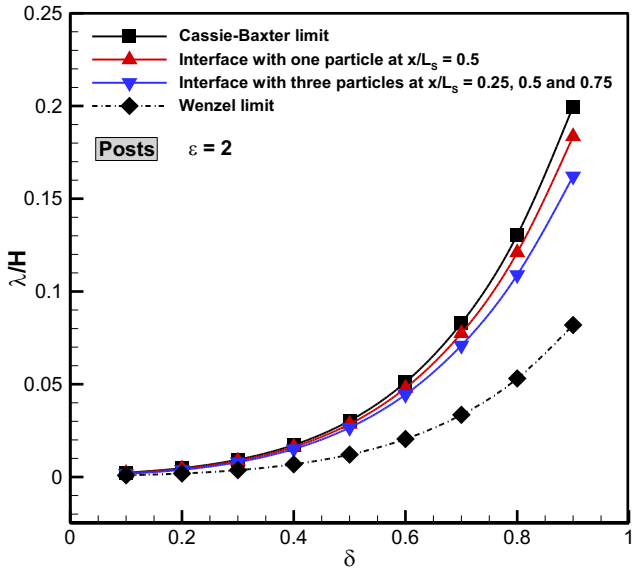

(a)

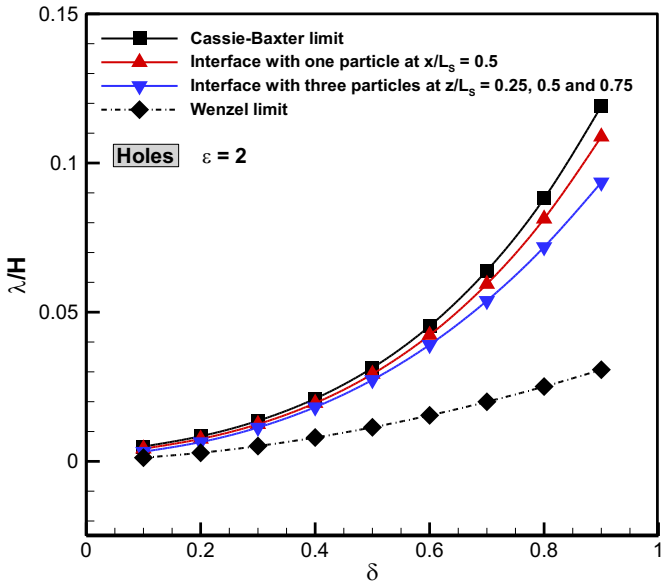

(b)

Figure 12: Variation of the effective slip length with gas fraction for flow in the Cassie-Baxter state (black squares), the Wenzel state (black diamonds), an interface with one particle (red triangles) and three particles (blue inverted triangles) for (**a)** posts and (**b)** holes. The constriction ratio is 2 in both the cases. Note that numerical simulations in the Wenzel state were carried out at $h/H = 0.5$ for both cases.

The effective slip length for posts and holes is plotted in Fig. 12 with respect to gas fraction. The effective slip length in the Cassie-Baxter state and the Wenzel state is also included in the figure as limiting cases. The effective slip length shows a dual behaviour for single-wall textured microchannels i.e., the effective slip length in the Wenzel state exceeds Cassie-Baxter state and vice versa based on the gas fraction and gas cavity height[46]. Therefore, the gas cavity dimensions are chosen according to $h/H = 0.5$ for simplicity, in those simulations where the flow exist in the Wenzel state. As seen from Fig. 12, an increase in number of adsorbed particles decreases the effective slip length for both posts and holes. Unlike the transverse ribs, the curves representing the effective slip length for 'dirty' interfaces are closer to the upper limit of the effective slip length. However, the percentage decrease in the no-shear area due to adsorbed particles is < 1% in all the cases for bi-dimensional textures. Therefore, the effective slip length data is expressed in the form of the slip loss in Fig. 13.

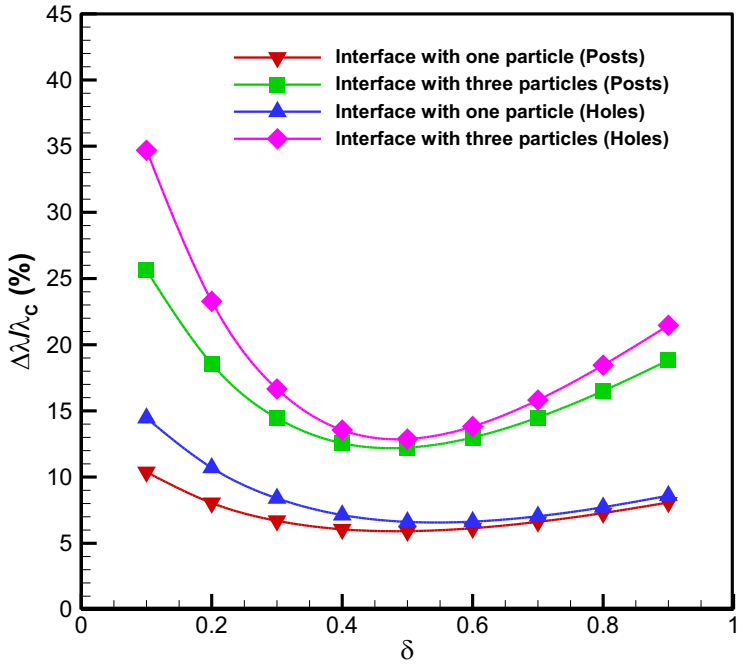

Figure 13: Percentage reduction in effective slip length versus gas fraction for posts and holes.

The slip loss shows a non-monotonic variation with respect to gas fraction, reaching a minima at $\delta = 0.5$ for both posts and holes. Similarly, the minimum is found to shift towards a larger gas fraction with a decrease in number of particles. A similar non-monotonic variation of the slip loss is also evident for traverse ribs in Fig. 3(b). Since posts consist of a continuous no-shear area along the flow direction unlike holes, the liquid experiences less intense acceleration-deceleration cycles. Therefore, the slip loss is more in the case of holes than posts. It is interesting to note that the slip loss is also significant for bi-dimensional textures (5 - 35%) for a negligible reduction in the no-shear area due to the adsorbed particles.

4.3 Influence of orientation of particle-ensemble

In order to appreciate the effect of acceleration-deceleration cycles on the slip loss in three-dimensional flows, the simulations were carried out for the geometry with holes by varying the orientation of the particle ensemble. In the first case, particles were arranged on an interface along the flow direction (X) and in the second case, particles were arranged normal to the flow direction (Z), as shown in the inset of Fig. 14. In both the cases, the particles are arranged equidistantly along particular directions.

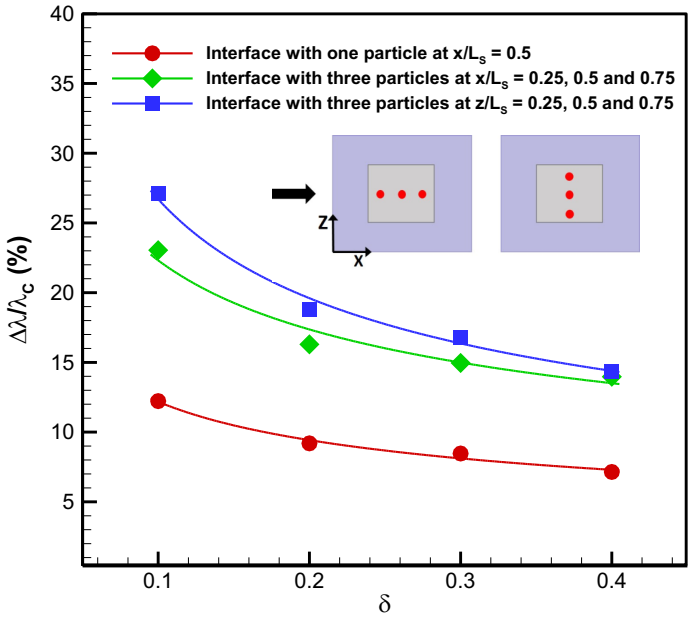

Figure 14: Effect of orientation of the particle ensemble on the percentage reduction in the effective slip length for holes. A graphic representing the particle ensemble orientation is shown in the inset with the flow direction marked (black arrow).

Fig. 14 shows the slip loss in both the cases mentioned earlier with respect to gas fraction. The slip loss caused by a single adsorbed particle at $x/L_S = 0.5$ is also added for comparison in the figure. The particle-ensemble arranged normal to the flow direction splits the distribution of interfacial velocity, thereby allowing the liquid to undergo two acceleration-deceleration cycles. However, the particle-ensemble arranged along the flow direction results in one acceleration-deceleration cycle on either side at the interface. Therefore, the slip loss is shown to be more in the former than the latter.

4.4 Validity of scaling laws

Ybert et al.[12] expressed scaling laws for the normalized effective slip length, both in the dilute ($\delta \rightarrow 0$) and dense ($\delta \rightarrow 1$) limits of the gas fraction, for various texture configurations including posts and holes. For instance, the scaling laws for the normalized effective slip length for shear flow past posts and holes respectively in the dilute limit is expressed as:

$$\left[\frac{\lambda}{L}\right]_{Posts} = A\delta^{B}, \tag{13}$$

$$\left[\frac{\lambda}{L}\right]_{Holes} = C\delta^{D}. \tag{14}$$

The constants A and B for posts in the limit of a large constriction ratio ($\varepsilon >> 1$) in the Stokes regime are 0.21 and 2 respectively. Similarly, the constants C and D for holes under the above conditions are 0.17 and 1.5 respectively. The constants of scaling laws were shown to be a function of Reynolds number in previous works[14]. Further, the value of the constants were shown to be decreasing with an increase in Re. In another study[25], the authors expressed that viscous dissipation effects in a textured microchannel alters the values of the constants in scaling relationships.

Table-2: Value of coefficients in Eq. 13 for 'clean' and 'dirty' interfaces for posts.

	'Clean' interface		Interface with one solid particle	
	A	B	A_P	B_P
$\varepsilon = 0.5$	0.464	2.117	0.439	2.118
$\varepsilon = 1$	0.255	2.175	0.240	2.176
$\varepsilon = 2$	0.130	2.178	0.124	2.179

Table-3: Value of coefficients in Eq. 14 for 'clean' and 'dirty' interfaces for holes.

	'Clean' interface		Interface with one solid particle	
	C	D	C_P	D_P
$\varepsilon = 0.5$	0.317	1.488	0.304	1.524
$\varepsilon = 1$	0.174	1.531	0.167	1.569
$\varepsilon = 2$	0.084	1.560	0.088	1.599

A particle positioned on a liquid-gas interface creates a three-phase constant line around the periphery (junction of the no-slip and no-shear regions), where an additional viscous dissipation occurs. This could lead to a change in the value of the constants in Eqs. 13 and 14. To validate this, simulations were carried out on the posts and holes configurations at different constriction ratios in the dilute limit of gas fraction ($\delta \leq 0.4$) with a single adsorbed particle. The particle was positioned on the interface at $x/L_S = 0.5$ with $\theta_{CA} = 90^o$ in the simulations. Fig. 15 shows the variation of the effective slip length at different constriction ratios for 'clean' and 'dirty' interfaces for posts and holes respectively. To avoid the overlapping of the normalized effective slip length curves, the data is represented in the form of the effective slip length for clarity. In the first instance, it is interesting to note that the scaling laws can be extended to single-wall textured microchannels. Further, the linearity of the effective slip length with gas fraction for a 'dirty' interface ensures that the scaling laws do indeed account for viscous dissipation effects. The value of the coefficients in the scaling laws for posts and holes are listed in tables 2 and 3 respectively for both 'clean' and 'dirty' interfaces. The value of the primary coefficients (A and C) for a 'clean' interface reduce, while the value of the secondary coefficients (B and D) increase, with an increase

in constriction ratio for both posts and holes. The variation of these constants in the above manner tends to reduce the effective slip length. In other words, as the constriction ratio decreases viscous dissipation increases in a textured microchannel, which results in a drop in the value of the effective slip length. A similar trend (i.e., variation in the value of the coefficients, A_P, B_P, C_P, and D_P) is also observed for a 'dirty' interface, as shown in tables 2 and 3. This indicates that the additional viscous dissipation caused by the adsorbed particle tends to reduce the effective slip length.

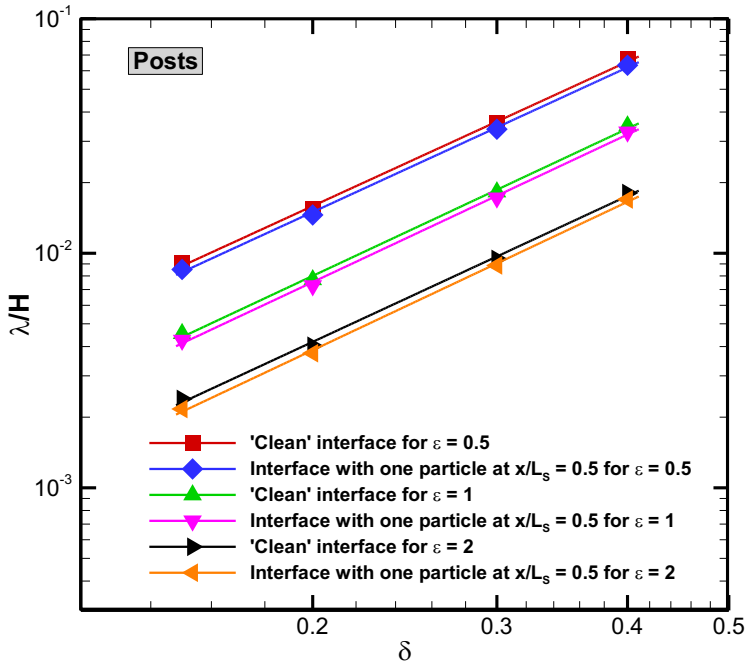

(a)

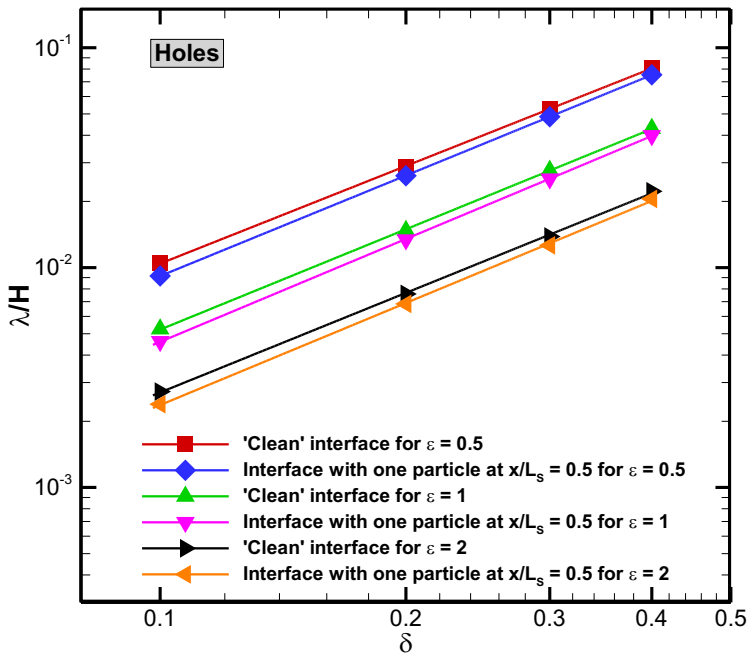

(b)

Figure 15 (a-b): Variation of the effective slip length with gas fraction for flow in the Cassie-Baxter state, and for an interface with a particle at different constriction ratios, for (**a)** posts and (**b)** holes.

5. CONCLUSIONS

In this work, the flow through a textured microchannel with an interface contaminated by solid particles was simulated. In the first part of this study, transverse ribs with one cylindrical particle on the liquid-gas interface was considered. The induced reduction in the effective slip length as a function texture geometry related parameters (gas fraction and constriction ratio) and particle related parameters (position and contact angle on an interface) was determined. In the second part, simulations were carried out for configurations of a two-dimensional textured surface containing posts or holes, with one or spherical particles situated on the liquid-gas interface. The validity of scaling laws for a particle-laden interface was examined. The main conclusions of this work are presented below:

1. For transverse ribs, it was observed that a particle adsorbed on the liquid-gas interface enforces the liquid to experience additional acceleration-deceleration cycles on the

interface. This leads to a reduction in the average slip velocity, and thus the effective slip length. Further, the effect of just a single adsorbed particle on the slip loss is significant (~ 20 - 80%) even though the reduction in the no-shear area is marginal (≤ 10%).

2. The slip loss was observed to be more in textured microchannels with a large constriction ratio ($\varepsilon \geq 1$). A larger slip on the liquid-gas interface at small constriction ratio reduces the detrimental effects of adsorbed particles.
3. Even a moderate increase in the number of particles on an interface drastically reduces the average slip velocity. Therefore, a textured microchannel with a particle-laden liquid-gas interface was observed to be ineffective in reducing slip as compared to a completely-wetted textured microchannel.
4. For a two-dimensional textured surface, a bounded particle-laden liquid-gas interface intensifies acceleration-deceleration cycles on the interface. Therefore, the slip loss was observed to be more for a surface with holes than posts. Further, the orientation of the particle ensemble on a liquid-gas interface signifies the importance of acceleration-deceleration cycles in increasing slip loss.
5. The variation in the computed values of coefficients in the scaling laws for particle-laden interfaces was attributed to viscous dissipation at the three-phase contact line around the periphery of the particle.

References

1. C. H. Choi, K. J. A. Westin, and K. S. Breuer, "Apparent slip flows in hydrophilic and hydrophobic microchannels," Phys. Fluids, **15**, 2897, (2003).
2. P. Joseph, C. Cottin-Bizonne, J. M. Benoît, C. Ybert, C. Journet, P. Tabeling, and L. Bocquet, "Slippage of water past superhydrophobic carbon nanotube forests in microchannels," Phys. Rev. Lett., **97**, 156104, (2006).
3. J. R. Philip, "Flows satisfying mixed no-slip and no-shear conditions," Angew. Math. Phys., **23**, 353 (1972).

4. C. Cottin-Bizonne, C. Barentin, E. Charlaix, L. Bocquet, and J. L. Barrat, “Dynamics of simple liquids at heterogeneous surfaces: molecular-dynamics simulations and hydrodynamic description,” Eur. Phys. J. E, **15**, 427, (2004).
5. A. Busse, N. D. Sandham, G. McHale and M. I. Newton, M. I. “Change in drag, apparent slip and optimum air layer thickness for laminar flow over an idealised superhydrophobic surface,” J. Fluid Mech, **727**, 488-508, (2013).
6. C. L. M. H. Navier, “Memoire sur les lois du movement des fluids,” Memoires de l’Academie Royale des Sciences de l’Institut de France **6**, 389 (1823).
7. K. Watanabe, Y. Udagawa, and H. Udagawa, “Drag reduction of Newtonian fluid in a circular pipe with a highly water-repellent wall,” J. Fluid Mech., **381**, 225–238 (1999)
8. R. Pit, H. Hervet, and L. Le´ger, “Direct experimental evidence of slip in Hexadecane: Solid interfaces,” Phys. Rev. Lett., **85**, 980 (2000)
9. J. L. Barrat, and L. Bocquet, “Large slip effect at a non-wetting fluid-solid interface,” Phys. Rev. Lett., **82**, 4671–4674 (1999)
10. C. H. Choi, U. Ulmanella, J. Kim, C. M. Ho, and C. J. Kim, C. J. “Effective slip and friction reduction in nano-grated superhydrophobic microchannels,” Phys. Fluids, **18**, 087105, (2006).
11. E. Lauga, and H. A. Stone, “Effective slip in pressure-driven Stokes flow,” J. Fluid Mech., **489**, 55–77 (2003)
12. C. Ybert , C. Barentin and C. Cottin-Bizonne, “Achieving large slip with superhydrophobic surfaces: scaling laws for generic geometries, ” Phys. Fluids, **19** 123601(2007)
13. B. Woolford, D. Maynes, and B. W. Webb. "Liquid flow through microchannels with grooved walls under wetting and superhydrophobic conditions," Microfluid Nanofluid, **7** 121-135, (2009).
14. Y. P. Cheng, C. J. Teo, and B. C. Khoo , “Microchannel flows with superhydrophobic surfaces: Effects of Reynolds number and pattern width to channel height ratio,” Phys. Fluids, **21**, 122004 (2009)
15. T. V. Nizkaya, E. S. Asmolov, and O. I. Vinogradova, “Gas cushion model and hydrodynamic boundary conditions for superhydrophobic textures,” Phys. Rev. E **90**, 043017 (2014)

16. D. Crowdy, “Slip length for longitudinal shear flow over a dilute periodic mattress of protruding bubbles,” Phys. Fluids, **22**, 121703 (2010).
17. A. M. J. Davis, and E. Lauga, “Geometric transition in friction for flow over a bubble mattress,” Phys. Fluids, **21**, 011701 (2009).
18. A. Steinberger, C. Cottin-Bizonne, P. Kleimann, and E. Charlaix, “High friction on a bubble mattress,” Nature Mater., **6**, 665 (2006).
19. J. Hyväluoma, and J. Harting, “Slip flow over structured surfaces with entrapped microbubbles,” Phys. Rev. Lett., **100**, 246001 (2008).
20. E. Karatay, A. S. Haase, C. W. Visser, C. Sun, D. Lohse, P. A. Tsai, and R. G. Lammertink, “Control of slippage with tunable bubble mattresses,” Proc. Nat. Acad. Sci. Usa, **110**, 8422-8426 (2013).
21. C. Lee, C. -H Choi, and C. -J Kim, “Structured surfaces for a giant liquid slip,” Phys. Rev. Lett., **101**,064501 (2008).
22. P. Tsai, A. M. Peters, C. Pirat, M. Wessling, R. G. H. Lammertink, and D. Lohse, “Quantifying effective slip length over micropatterned hydrophobic surfaces,” Phys. Fluids, **21**, 112002, (2009).
23. T. J. Kim and C. Hidrovo, “Pressure and partial wetting effects on superhydrophobic friction reduction in microchannel flow,” Phys. Fluids, **24**, 112003, (2012).
24. A. Gaddam, A. Agrawal, S. S. Joshi, and M. C. Thompson, “Utilization of cavity vortex to delay the wetting transition in one-dimensional structured microchannels”, Langmuir, **31**, 13373−13384 (2015).
25. A. Gaddam, K.S. Bharath, A. Agrawal and S. S. Joshi “Demarcating wetting states in textured microchannels under flow conditions by Poiseuille number,” Microfluid Nanofluid, **21**, 137 (2017).
26. G. Bolognesi, C. Cottin-Bizonne, and C. Pirat, “Experimental evidence of slippage breakdown for a superhydrophobic surface in a microfluidic device,” Phys. Fluids, **26**, 082004 (2014).
27. W. Zheng, L. P. Wang, D. Or, V. Lazouskaya, and Y. Jin, “Role of mixed boundaries on flow in open capillary channels with curved air-water interfaces”, Langmuir, **28**, 12753 −12761 (2012).

28. D. Schäffel, K. Koynov, D. Vollmer, H. J. Butt, and C. Schönecker, "Local flow field and slip length of superhydrophobic surfaces," Phys. Rev. Lett, **116(13)**, 134501 (2016).
29. O. Manor, I. U. Vakarelski, G. W. Stevens, F. Grieser, R. R. Dagastine, and D. Y. Chan, "Dynamic forces between bubbles and surfaces and hydrodynamic boundary conditions," Langmuir, **24**, 11533, (2008).
30. C. L. Henry, L. Parkinson, J. R. Ralston, and V. S. Craig, "A mobile gas−water interface in electrolyte solutions," J. Phys. Chem. C, **112**, 15094, (2008).
31. S. Tripathi, A. Kumar, Y. B. V. Kumar, and A. Agrawal "Three-dimensional hydrodynamic flow focusing of dye, particles and cells in a microfluidic device by employing two bends of opposite curvature," Microfluid Nanofluid, **20**, 1, (2016).
32. T. Sawetzki, S. Rahmouni, C. Bechinger, and D. W. Marr, "In situ assembly of linked geometrically coupled microdevices," Proc. Natl. Acad. Sci. U.S.A., **105**, 20141, (2008).
33. X. Wu, H. Wu, and P. Cheng, "Pressure drop and heat transfer of Al2O3-H2O nanofluids through silicon microchannels," J. Micromech. Microeng, **19**, 105020, (2009).
34. B. P. Binks, and T. S. Horozov, (Eds.). "Colloidal particles at liquid interfaces," Cambridge University Press, (2006).
35. A. Vidal, and L. Botto, "Slip flow past a gas–liquid interface with embedded solid particles," J. Fluid Mech., **813**, 152, (2017).
36. C. J. Teo, and B. C. Khoo, "Analysis of Stokes flow in microchannels with superhydrophobic surfaces containing a periodic array of micro-grooves," Microfluid Nanofluid, **7**, 353, (2009).
37. J. Happel, and H. Brenner, "Low Reynolds number hydrodynamics: with special applications to particulate media (Vol. 1)," Springer Science & Business Media, (2012).
38. A. Gaddam, M. Garg, A. Agrawal, and S.S. Joshi, "Modeling of liquid-gas meniscus for textured surfaces: Effect of curvature and local slip length," J. Micromech. Microeng., **25**, 125002 (2015).
39. J. Davies, D. Maynes, B. W. Webb, and B. Woolford, "Laminar flow in a microchannel with superhydrophobic walls exhibiting transverse ridges," Phys. Fluids, **18**, 087110 (2006).
40. M. Zanini, and L. Isa, "Particle contact angles at fluid interfaces: pushing the boundary beyond hard uniform spherical colloids," J. Phys. Condens. Matter, **28**, 313002, (2016).

41. T. M. Ruhland, A. H. Gröschel, N. Ballard, T. S. Skelhon, A. Walther, A. H. Müller, and S. A. Bon, "Influence of Janus particle shape on their interfacial behavior at liquid–liquid interfaces," Langmuir, **29**, 1388, (2013).
42. T. M. Ruhland, A. H. Gröschel, A. Walther, and A. H. Müller, "Janus cylinders at liquid–liquid interfaces," Langmuir, **27**, 9807, (2011).
43. R. Enright, M. Hodes, T. Salamon, and Y. Muzychka, "Isoflux Nusselt number and slip length formulae for superhydrophobic microchannels," J. Heat Transfer., **136**, 012402, (2014).
44. A. Cowley, D. Maynes, and J. Crockett, "Inertial effects on thermal transport in superhydrophobic microchannels," Int J Heat Mass Trans., **101**, 121, (2016).
45. A. Dörr, S. Hardt, H. Masoud, and H. A. Stone, "Drag and diffusion coefficients of a spherical particle attached to a fluid–fluid interface," J. Fluid Mech., **790**, 607, (2016).
46. A. Lee, H. -Y. Kim, "Does liquid slippage within a rough channel always increase the flow rate?" Phys. Fluids, **26**, 072002 (2014).